ELSEVIER

International Journal of Mass Spectrometry 185/186/187 (1999) 117–129

International Journal of Mass Spectrometry

Oxidation of CO and reduction of CO_2 by gas phase Zr^+, ZrO^+, and ZrO_2^+

M.R. Sievers, P.B. Armentrout*

Department of Chemistry, University of Utah, Salt Lake City, UT 84112, USA

Received 12 May 1998; accepted 1 July 1998

Abstract

Guided ion beam mass spectrometry is used to investigate the kinetic energy dependence of the reactions of Zr^+ (^4F) and ZrO^+ ($^2\Sigma^+$) with CO_2, and the reverse pathways, ZrO^+ ($^2\Sigma^+$) and ZrO_2^+ with CO. To further probe these reaction systems, the intermediates, $OZr(CO)^+$, $OZr(CO_2)^+$, and $O_2Zr(CO)^+$ are studied by collisional activation experiments with Xe. Thermochemical analysis of the reaction cross sections obtained in this study yield (in eV) $D_0(Zr^+\text{-}CO) = 0.80 \pm 0.10$, $D_0(OZr^+\text{-}CO) = 0.84 \pm 0.08$, $D_0(OZr^+\text{-}CO_2) = 0.74 \pm 0.06$, $D_0(O_2Zr^+\text{-}CO) = 1.01 \pm 0.08$, and $D_0(OZr^+\text{-}O) = 3.86 \pm 0.07$. Speculative determinations of electronic excitation energies for two states of ZrO^+ are also made. (Int J Mass Spectrom 185/186/187 (1999) 117–129) © 1999 Elsevier Science B.V.

Keywords: Zirconium ions; Zirconium oxide ions; Carbon dioxide; CO oxidation; Bond energies; Guided ion beam mass spectrometry

1. Introduction

The use of metals and metal oxides as catalysts is an active field of study [1–10]. Previous work on zirconium has focused on the utilization of copper–zirconium alloys [11], supported ZrO_2 [12,13], and unsupported ZrO_2 [14,15] as hydrogenation catalysts for CO and CO_2. Some insight into the thermodynamics and mechanisms of such systems may be obtained by studying the reactions of metal and metal oxide cations with CO or CO_2 in the gas phase [16–23]. Here, we examine the reactions of Zr^+ and ZrO^+ using a guided ion beam mass spectrometer, in direct analogy with previous studies of V^+ [24], Nb^+, and NbO^+ [25]. Such gas-phase work allows us to examine the kinetics and energetics of these reactions and probe the detailed interactions of Zr^+ and ZrO^+ with CO_2. In this study, both the forward and reverse reactions are examined and several intermediates are independently generated and characterized. Thermodynamic information for many of these species as well as speculative excitation energies for two excited states of ZrO^+ are determined.

A very important consideration in the systems studied here is the electronic states of the metal, metal monoxide, and metal dioxide cations. The ground state of Zr^+ is $a^4F(5s^14d^2)$ with low lying excited states starting at energies (in eV) of 0.32 (b^4F, $4d^3$), 0.53 (a^2D, $5s^14d^2$), 0.71 (a^2P, $5s^14d^2$), 0.71 (a^2F, $5s^14d^2$), 0.93 (a^4P, $5s^14d^2$), and 0.97 (a^2G, $4d^3$) above the ground state [26]. The ground state for

* Corresponding author.

Dedicated to Professor Michael T. Bowers on the occasion of his 60th birthday and in honor of his many contributions to gas-phase ion chemistry.

PII S1387-3806(98)14074-5

ZrO^+ has been experimentally determined to be $^2\Sigma^+(\sigma^2\pi^4\sigma^1)$ [27,28], but no excited electronic state information is known to our knowledge. The ground state for the metal dioxide is unknown theoretically or experimentally, but theoretical calculations [29] on the isovalent YO_2 neutral molecule find it to have a $^2\Sigma^+$ ground state. Therefore it seems reasonable to believe that ZrO_2^+ also has a doublet ground state with a linear geometry. Overall, these considerations show that the reaction of ground state $Zr^+(^4F)$ + $CO_2(^1\Sigma_g^+)$ cannot form ground state $ZrO^+(^2\Sigma^+)$ + $CO(^1\Sigma^+)$ products in a spin-allowed process while $ZrO^+(^2\Sigma^+)$ + $CO_2(^1\Sigma_g^+)$ can form $ZrO_2^+(^2\Sigma^+)$ + $CO(^1\Sigma^+)$ in a spin-allowed process.

2. Experimental

2.1. General

These studies are performed using a guided ion beam tandem mass spectrometer. The instrument and experimental methods have been described previously [30,31]. Ions, formed as described below, are extracted from the source, accelerated, and focused into a magnetic sector momentum analyzer for mass analysis. The ions are decelerated to a desired kinetic energy and focused into an octopole ion guide that radially traps the ions. While in the octopole, the ions pass through a gas cell that contains the neutral reactant at pressures where multiple collisions are improbable (<0.30 m Torr). Single collision conditions were verified by examining the pressure dependence of the cross sections measured here. The product ions and the reactant ion beam drift out of the gas cell are focused into a quadrupole mass filter and then detected by a secondary electron scintillation detector. Ion intensities are converted to absolute cross sections as described previously [30]. Uncertainties in the absolute cross sections are estimated at ±20%.

To determine the absolute zero and distribution of the ion kinetic energy, the octopole is used as a retarding energy analyzer [30]. The uncertainty in the absolute energy scale is ±0.05 eV (lab). The full width at half-maximum (fwhm) of the ion energy distribution is 0.2–0.4 eV (lab). Lab energies are converted into center-of-mass energies using $E(\mathrm{CM}) = E(\mathrm{lab})m/(m + M)$ where M and m are the masses of the ion and neutral reactant, respectively. All energies stated in this article are in the center-of-mass frame, unless noted otherwise.

2.2. Ion source

The ion source used here is a dc discharge/flow tube (DC/FT) source described in previous work [31]. The DC/FT source utilizes a zirconium cathode held at 1.5–3 kV over which a flow of approximately 90% He and 10% Ar passes at a typical pressure of ~0.5 Torr. Ar^+ ions created in a direct current discharge are accelerated toward the zirconium cathode, sputtering off atomic metal ions. The ions then undergo ~10^5 collisions with He and ~10^4 collisions with Ar in the meter long flow tube before entering the guided ion beam apparatus. From results obtained previously [32], we believe that the ions produced in the DC/FT source are exclusively in their a^4F ground state, and we assume the populations of the spin–orbit levels have a Maxwell-Boltzmann distribution at 300 ± 100 K.

Ground state ZrO^+ and ZrO_2^+ were made by allowing Zr^+ (created in the dc discharge) to react with O_2 introduced ~25 cm downstream into the flow tube at ~2 m Torr. $OZr^+(CO)$ and $O_2Zr^+(CO)$ were produced by allowing the Zr^+ to react with O_2 upstream in the flow tube and CO downstream. $OZr^+(CO_2)$ was produced by allowing ZrO^+ to interact with CO_2 downstream in the flow tube. Three-body collisions with the He/Ar flow gas stabilize these species and the large number of collisions between the ions and the bath gases should thermalize the ions both rotationally and vibrationally. We assume that these ions are in their ground electronic states and that the internal energy of these clusters is well described by a Maxwell-Boltzmann distribution of rotational and vibrational states corresponding to 300 ± 100 K.

Previous work from this laboratory, including studies of N_4^+ [33], $Fe(CO)_x^+$ ($x = 1–5$) [34], $Cr(CO)_x^+$ ($x = 1–6$) [35], SiF_x^+ ($x = 1–4$) [36], and $H_3O^+(H_2O)_x$ ($x = 1–5$) [37] have shown that these assumptions are usually valid.

Attempts were made to produce $Zr^+(CO_2)$. Addition of CO_2 downstream in the flow tube did produce a cation which had the mass of $Zr^+(CO_2)$. To determine the identity of this species, CID experiments were performed on this complex cation and the results indicated that the ion formed had the $OZr^+(CO)$ structure rather than being the CO_2 ligated zirconium cation. In addition, ligand exchange reactions between $Zr^+(N_2)$ and CO_2 in the flow tube did not form any species that behaved as though it had the $Zr^+(CO_2)$ structure.

Table 1
Molecular vibrational frequencies

Species		Frequencies (cm^{-1})[a]
ZrO^+[b]		1114
ZrO_2^+[b]		502(2), 813, 960
CO_2[c]		667(2), 1333, 2349
CO[d]		2214.2
$OZr^+(CO)$	(1)[b]	35(2), 166, 221(2) + $\nu(ZrO^+)$ + ν(CO)
	(2)[b]	20(2), 100, 150(2) + $\nu(ZrO^+)$ + ν(CO)
$OZr^+(CO_2)$	(1)[b]	150(2), 200(2) + $\nu(ZrO^+)$ + $\nu(CO_2)$
	(2)[e]	25, 105, 196, 200, 600, 935, 1067, 1176, 1745
$O_2Zr^+(CO)$	(1)[b]	20(2), 100, 150 + $\nu(ZrO_2^+)$ + ν(CO)
	(2)[b]	35(2), 166, 221 + $\nu(ZrO_2^+)$ + ν(CO)

[a]Numbers in parentheses denote the degeneracy of the vibration.
[b]See text for discussion.
[c][44].
[d][45].
[e]$V^+(CO_2)$ frequencies from [24] and estimates for two bends (25 and 200 cm^{-1}).

2.3. Data analysis

Previous theoretical [38,39] and experimental work [40] has shown that endothermic cross sections can be modeled using Eq. (1),

$$\sigma(E) = \sigma_0 \sum g_i (E + E_{rot} + E_i - E_0)^n/E \quad (1)$$

where σ_0 is an energy independent scaling parameter, E is the relative translational energy of the reactants, E_{rot} is the average rotational energy of the reactants, E_0 is the reaction threshold at 0 K, and n is an energy independent scaling parameter. The summation is over each vibrational state of the reactants having relative populations g_i and energies E_i. The various sets of vibrational frequencies used in this work are listed in Table 1. The vibrational frequency for ZrO^+ was estimated by Morse potential scaling [i.e. $\omega_1/\omega_2 = (\mu_2/D_{e2})^{1/2}/(\mu_1/D_{e1})^{1/2}$ [41] of the NbO^+ frequency taken from the study of Dyke et al. [42]. Frequencies for ZrO_2^+ were estimated to equal frequencies measured from electron diffraction work on NbO_2 after scaling by a Morse potential [43]. The additional frequency that is needed for the linear geometry is estimated by doubling the degeneracy of the lowest frequency. The frequencies for CO and CO_2 were taken from the literature [44,45] The vibrational frequencies for $OZr^+(CO)$, $O_2Zr^+(CO)$, and $OZr^+(CO_2)$ were taken to equal the vibrational frequencies of ZrO^+ or ZrO_2^+, and CO or CO_2, plus sets of frequencies for the metal oxide–ligand modes that are similar to those we have used previously for $CrCO^+$ and $V^+(CO_2)$ [24,35]. The frequencies used in this study are estimates and therefore were varied by ±20% in the data analysis. This frequency variation is reflected in the uncertainties reported for the fitting parameters in Eq. (1).

Before comparison with the data, the model of Eq. (1) is convoluted over the neutral and ion kinetic energy distributions using previously developed methods [30]. The parameters E_0, σ_0, and n are then optimized using a nonlinear least squares analysis in order to best reproduce the data. Reported values of E_0, σ_0, and n are mean values for each parameter from the best fits to several independent sets of data and uncertainties are one standard deviation from the mean. The listed uncertainties in the E_0 values also include the uncertainty in the absolute energy scale and uncertainties introduced by the estimated vibrational frequencies used for the various complexes studied.

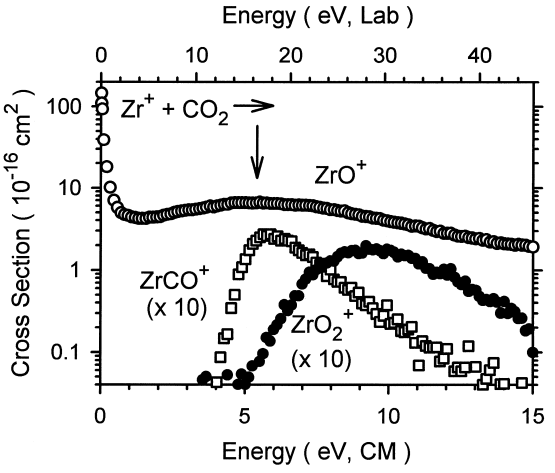

Figure 1. Product cross sections for $Zr^+ + CO_2$ as a function of collision energy in the center of mass frame (lower *x* axis) and laboratory frame (upper *x* axis). The arrow marks the bond dissociation energy of CO_2 at 5.45 eV.

3. Results

3.1. $Zr^+ + CO_2$

Zirconium cations react with carbon dioxide to form three products in reactions (2)–(4), as shown in Fig. 1.

$$Zr^+ + CO_2 \rightarrow ZrO^+ + CO \quad (2)$$

$$\rightarrow ZrCO^+ + O \quad (3)$$

$$\rightarrow ZrO_2^+ + C \quad (4)$$

Literature thermochemistry shown in Table 2 establishes that reaction (2) is exothermic by 2.31 ± 0.11 eV. The ZrO^+ cross section does show exothermic reaction behavior up to near 1 eV. Indeed, a model with an energy dependence of $E^{-1.0 \pm 0.1}$ reproduces the data to a kinetic energy of about 0.75 eV, as shown in Fig. 2. Above this energy, the cross section then begins to rise until near 5.5 eV where it starts to decrease again. This behavior is characteristic of the onset of reaction (5), dissociation of ZrO^+,

$$Zr^+ + CO_2 \rightarrow Zr^+ + CO + O \quad (5)$$

which can begin at D_0(OC-O), Table 2. In the intermediate energy region, the ZrO^+ cross section can be reproduced by introducing an additional model with optimum parameters of Eq. (1) given in Table 3. The sum of these two models reproduces the ZrO^+ cross section accurately up to 5 eV as shown in Fig. 2. The threshold for this endothermic feature is attributed to formation of an excited state of ZrO^+. This conclu-

Table 2
Bond dissociation energies at 0 K

Bond	Bond energy (eV)
C-O	11.108 ± 0.005[a]
OC-O	5.453 ± 0.002[a]
Zr^+-O	7.76 ± 0.11[b]
Zr^+-CO	0.89 ± 0.13,[c] 0.80 ± 0.10[d]
OZr^+-O	3.5 ± 0.4,[e] 3.86 ± 0.07[d]
OZr^+-CO	0.84 ± 0.08[d]
OZr^+-CO_2	0.74 ± 0.06[d]
O_2Zr^+-CO	1.01 ± 0.08[d]

[a]Calculated from data in S.G. Lias, J.E. Bartmess, J.F. Liebman, J.L. Holmes; R.D. Levin, W.G. Mallard, J. Phys. Chem. Ref. Data 17 (1988) (suppl. 1).
[b][48].
[c][47].
[d]This work
[e][49].

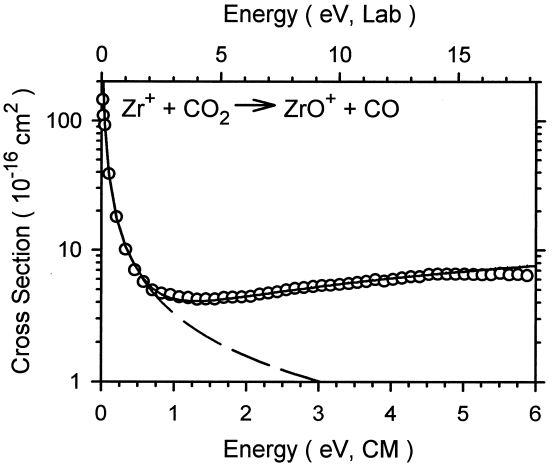

Figure 2. Product cross section for $Zr^+ + CO_2$ to form $ZrO^+ + CO$ in the threshold region as a function of collision energy in the center of mass frame (lower *x* axis) and laboratory frame (upper *x* axis). The dashed line shows a model for exothermic formation of ZrO^+. The solid line shows the sum of this model and one for endothermic formation of ZrO^+ after being convoluted with the experimental energy distributions. The optimized parameters used in Eq. (1) for the endothermic model are listed in Table 3.

Table 3
Optimized parameters of Eq. (1) for $ZrCO_2^+$ system

Reaction		σ_0	n	E_0, eV
$Zr^+ + CO_2$	$\rightarrow ZrO^+ + CO$	3.44 (0.31)	1.5 (0.1)	0.62 (0.08)
	$\rightarrow ZrCO^+ + O$	1.56 (0.28)	0.1 (0.2)	4.65 (0.10)
	$\rightarrow ZrO_2^+ + C$	0.082 (0.034)	2.3 (0.3)	4.92 (0.21)
$ZrO^+ + CO$	$\rightarrow Zr^+ + CO_2$	0.0023 (0.0013)	2.5 (0.3)	2.53 (0.31)
	$\rightarrow Zr^+ + O + CO$	0.053 (0.026)	3.1 (0.3)	7.87 (0.21)
	$\rightarrow ZrO_2^+ + C$	0.35 (0.10)	2.3 (0.2)	7.80 (0.13)
$OZr^+(CO) + Xe$	$\rightarrow ZrO^+ + CO + Xe$	15.2 (1.6)	2.0 (0.2)	0.84 (0.08)

sion is in direct analogy with results for reactions of V^+ and $Nb^+ + CO_2$ [24,25] where knowledge of the associated excited states was available from photoelectron spectroscopy [42,46].

The formation of $ZrCO^+$ begins near 4 eV and reaches a maximum near $D_0(OC–O)$, indicating that its decline is due to reaction (5), dissociation of the $ZrCO^+$ product. The threshold measured for this cross section (Table 3) corresponds to $D_0(Zr^+\text{-}CO) = 0.80 \pm 0.10$ eV. This compares favorably with a theoretically calculated value of 0.89 ± 0.13 eV, Table 2 [47]. Formation of ZrO_2^+ in reaction (4) is not observed until an apparent threshold near 5 eV. This ion can dissociate to form $ZrO^+ + O$, beginning at 8.80 ± 0.11 eV, or to $Zr^+ + O_2$, beginning at 11.44 eV. The elevated threshold and competition with the much more favorable reaction (2) explain the small sizes of the cross sections for reactions (3) and (4). Analysis of the $ZrO_2{}^+$ cross section gives a threshold of 4.92 ± 0.21 eV (Table 3). This can be combined with the atomization energy of CO_2, 16.56 eV, and $D_0(Zr^+\text{-}O) = 7.76 \pm 0.11$ eV (Table 2) to give $D_0(OZr^+\text{-}O) = 3.88 \pm 0.24$ eV.

3.2. $ZrO^+ + CO$

The reaction of ZrO^+ and CO, shown in Fig. 3, forms two products in reactions (6)–(8).

$$ZrO^+ + CO \rightarrow Zr^+ + CO + O \quad (6)$$

$$\rightarrow Zr^+ + CO_2 \quad (7)$$

$$\rightarrow ZrO_2^+ + C \quad (8)$$

The Zr^+ cross section rises slowly from an apparent threshold near 3 eV until near 8 eV at which point it increases more rapidly. The latter feature corresponds to reaction (6), simple collision-induced dissociation, which can begin at $D_0(Zr^+\text{-}O)$, Table 2. Therefore the lower energy feature must correspond to reaction (7), the reverse of reaction (2), and can be reproduced using Eq. (1) and the parameters in Table 3. The threshold obtained, 2.53 ± 0.31 eV, is consistent with formation of ground state Zr^+ (a^4F) at 2.31 eV, Zr^+ (b^4F) at 2.63 eV, or Zr^+ (a^2D) at 2.84 eV. The uncertainty in the measurement does not allow an

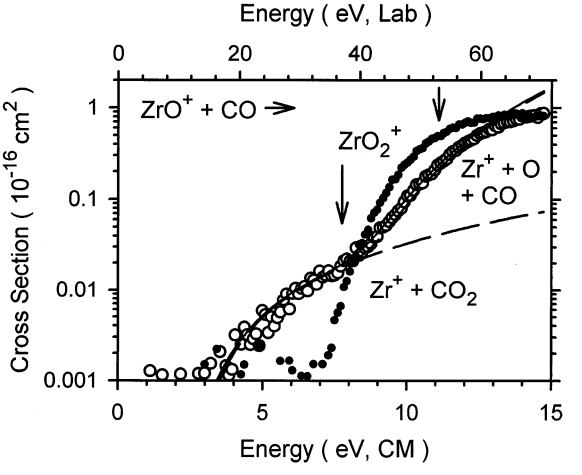

Figure 3. Product cross sections for $ZrO^+ + CO$ as a function of collision energy in the center-of-mass frame (lower x axis) and laboratory frame (upper x axis). Arrows mark the bond dissociation energies of ZrO^+ at 7.76 eV and CO at 11.11 eV. The dashed lines are the model of Eq. (1) with the optimized parameters listed in Table 3 for the formation of $Zr^+(b^4F) + CO_2$ and $Zr^+ + O + CO$. The solid line shows the sum of these two models convoluted over the experimental energy distributions.

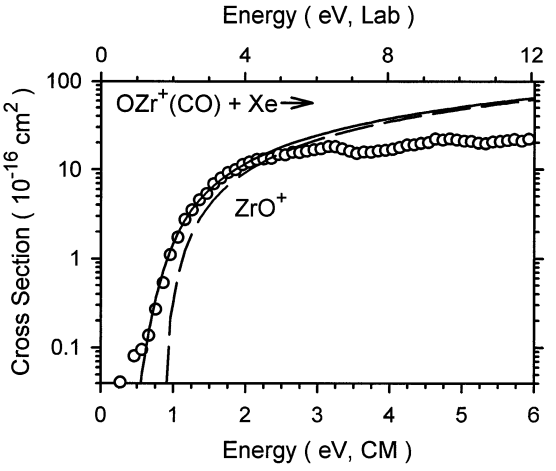

Figure 4. Product cross sections for $OZr^+(CO) + Xe$ as a function of collision energy in the center-of-mass frame (lower *x* axis) and laboratory frame (upper *x* axis). The dashed line shows the model of Eq. (1) with optimized parameters in Table 3. The solid line is this model convoluted over the experimental energy distributions.

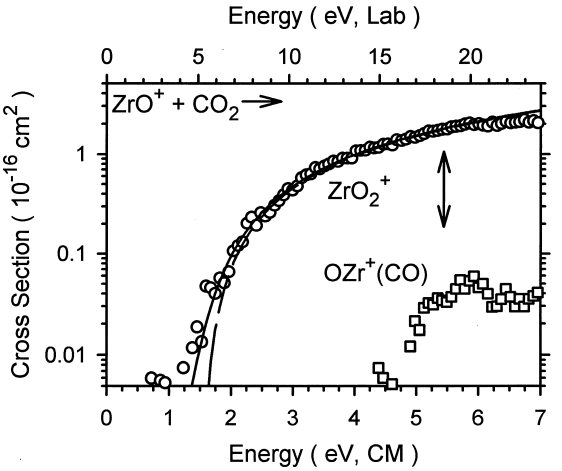

Figure 5. Product cross sections for $ZrO^+ + CO_2$ as a function of collision energy in the center-of-mass frame (lower *x* axis) and laboratory frame (upper *x* axis). The arrow marks the bond dissociation energy of CO_2 at 5.45 eV. The dashed line shows the model of Eq. (1) with optimized parameters shown in Table 4. The solid line is this model convoluted over the experimental energy distributions.

accurate assessment of which state is actually formed. This process is very inefficient, characterized by a small σ_0 value and a large *n* parameter. This inefficiency could be due to the spin forbidden nature of forming Zr^+ (^4F). The threshold extracted from our modeling of the higher energy feature (after subtracting the model for reaction (7) from the ZrO^+ cross section), 7.87 ± 0.21 eV (Table 3), corresponds well with $D_0(Zr^+\text{-}O)$, Table 2.

The ZrO_2^+ cross section starts to rise near 7 eV. It continues to increase until near 11 eV where the product can dissociate to ZrO^+ and O, starting at $D_0(CO)$. The measured threshold for reaction (8) of 7.80 ± 0.13 eV (Table 3) can be combined with $D_0(CO)$ to yield $D_0(OZr^+\text{-}O) = 3.31 \pm 0.13$ eV.

3.3. $OZr^+(CO) + Xe$

The collisional activation of $OZr^+(CO)$ with Xe yields the formation of only one product, ZrO^+, in reaction (9), as shown in Fig. 4.

$$OZr^+(CO) + Xe \rightarrow ZrO^+ + CO + Xe \quad (9)$$

The cross section rises from an apparent threshold near 0.5 eV until near 2 eV where it levels off. Analysis of this cross section with Eq. (1) yields the optimized parameters in Table 3. The threshold of 0.84 ± 0.08 eV is assigned to $D_0(OZr^+\text{-}CO)$, Table 2.

3.4. $ZrO^+ + CO_2$

Two products are observed for the reaction of ZrO^+ with CO_2, as shown in Fig. 5. These can be formed in reactions (10) and (11).

$$ZrO^+ + CO_2 \rightarrow ZrO_2^+ + CO \quad (10)$$

$$\rightarrow ZrCO_2^+ + O \quad (11)$$

The ZrO_2^+ product cross section rises from an apparent threshold near 1 eV and continues to rise rapidly until near 6 eV. Analysis of this cross section gives a threshold of 1.59 ± 0.07 eV (Table 4). Combined with $D_0(OC\text{-}O)$, this threshold yields $D_0(OZr^+\text{-}O) = 3.86 \pm 0.07$ eV. The $ZrCO_2^+$ product ion, which has a likely structure of $OZr^+(CO)$, has a small cross section that rises from an apparent threshold near 4.5 eV. The cross section continues to rise to near an

Table 4
Optimized parameters of Eq. (1) for the $ZrCO_3^+$ system

Reaction	σ_0	n	E_0, eV
$ZrO^+ + CO_2 \rightarrow ZrO_2^+ + CO$	0.64 (0.09)	2.0 (0.1)	1.59 (0.07)
$\rightarrow OZr^+(CO) + O$	0.44 (0.05)	1.5 (0.4)	4.97 (0.09)
$ZrO_2^+ + CO \rightarrow ZrO^+ + CO_2$	1.99 (0.22)	1.2 (0.1)	0.40 (0.04)
	4.90 (0.09)	1.0 (0.1)	3.75 (0.14)
$OZr^+(CO_2) + Xe \rightarrow ZrO^+ + CO_2 + Xe$	21.6 (2.8)	1.8 (0.3)	0.74 (0.06)
$O_2Zr^+(CO) + Xe \rightarrow ZrO_2^+ + CO + Xe$	72.3 (7.2)	1.1 (0.4)	1.02 (0.08)
$ZrO_2^+ + Xe \rightarrow ZrO^+ + O + Xe$	0.63 (0.24)	1.9 (0.3)	3.97 (0.20)

energy consistent with the onset of reaction (12), D_0(OC-O), where it then declines slightly.

$$ZrO^+ + CO_2 \rightarrow ZrO^+ + CO + O \quad (12)$$

Analysis of the $ZrCO_2^+$ cross section gives a threshold of 4.97 ± 0.09 eV (Table 4). If the structure of the cation is OZr^+(CO), the threshold obtained for this channel can be combined with D_0(OC-O) to give $D_0(OZr^+\text{-}CO) = 0.48 \pm 0.09$ eV which is somewhat lower than the value obtained from reaction (9), 0.84 ± 0.08 eV. If the structure of the complex cation was that of a Zr^+ ligated with CO_2, the threshold obtained would yield $D_0(Zr^+\text{-}CO_2) = 2.79 \pm 0.14$ eV. This is much too large in comparison to $D_0(V^+\text{-}CO_2) = 0.75 \pm 0.04$ eV [24], indicating that the structure of OZr^+(CO) is more reasonable. The elevated threshold is probably a result of the severe competition with the much more favorable reaction (10).

3.5. $ZrO_2^+ + CO$

Figure 6 shows the ZrO^+ product formed from the interaction of ZrO_2^+ with CO in reactions (13) and (14). No other products were observed:

$$ZrO_2^+ + CO \rightarrow ZrO^+ + CO_2 \quad (13)$$

$$\rightarrow ZrO^+ + CO + O \quad (14)$$

The cross section shows exothermic reaction behavior with an energy dependence of $E^{-1.0 \pm 0.1}$ up to 0.5 eV, Fig. 6. The cross section then starts to rise slowly until about 3.5 eV at which point it begins to rise more rapidly. To reproduce the data up to 7 eV, the exothermic feature is combined with two models having optimum parameters given in Table 4. A single endothermic model cannot reproduce this higher energy portion of the cross section.

The observation of exothermic reaction behavior for process (13), the reverse of reaction (10), shows that $D_0(OZr^+\text{-}O) < D_0(OC\text{-}O) = 5.45$ eV. The higher energy endothermic feature of the cross section starting near 3.5 eV most likely corresponds to simple CID of ZrO_2^+, reaction (14). Therefore, the low energy endothermic feature must also correspond to

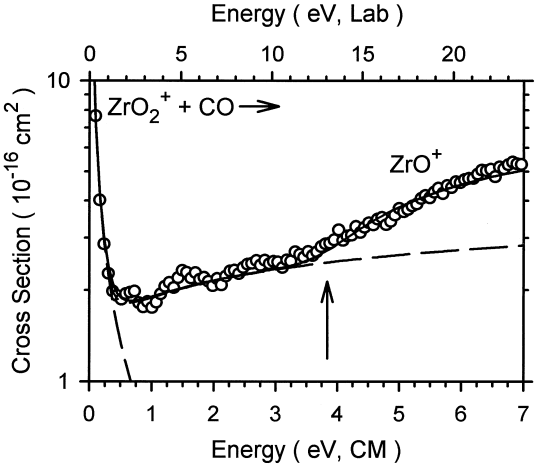

Figure 6. Product cross sections for $ZrO_2^+ + CO$ to form ZrO^+ as a function of collision energy in the center-of-mass frame (lower x axis) and laboratory frame (upper x axis). The dashed lines show a model for exothermic formation of ZrO^+ and the sum of this model and one for endothermic formation of ZrO^+. The full line shows the sum of these models with a second endothermic process after being convoluted over the experimental energy distributions. The optimized parameters used in Eq. (1) for the endothermic models are listed in Table 4. The arrow designates $D_0(OZr^+\text{-}O)$ at 3.86 eV.

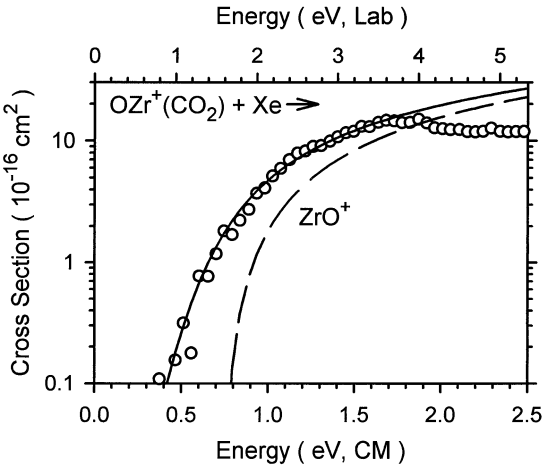

Figure 7. Product cross sections for $OZr^+(CO_2)$ + Xe as a function of collision energy in the center-of-mass frame (lower *x* axis) and laboratory frame (upper *x* axis). The dashed line shows the model of Eq. (1) with optimized parameters shown in Table 4. The solid line is this model convoluted over the experimental energy distributions.

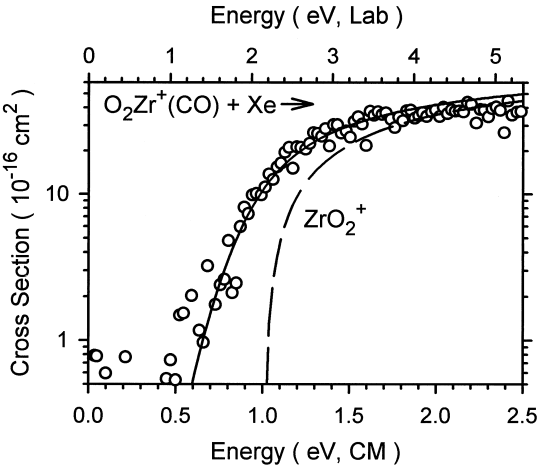

Figure 8. Product cross sections for $O_2Zr^+(CO)$ + Xe as a function of collision energy in the center-of-mass frame (lower *x* axis) and laboratory frame (upper *x* axis). The dashed line shows the model of Eq. (1) with optimized parameters shown in Table 4. The solid line is this model convoluted over the experimental energy distributions.

reaction (13) and is plausibly assigned to formation of ZrO^+ in an excited electronic configuration. It is possible that the observed threshold corresponds to a barrier to formation of excited state ZrO^+ rather than the asymptotic value.

3.6. $OZr^+(CO_2)$ + Xe

The collision-induced dissociation of the $OZr^+(CO_2)$ complex ion with Xe results in one product, shown in Fig. 7, formed by reaction (15).

$$OZr^+(CO_2) + Xe \rightarrow ZrO^+ + CO_2 + Xe \qquad (15)$$

The ZrO^+ cross section rises from an apparent threshold near 0.5 eV until near 1.5 eV at which point it levels off. The fact that the loss of CO_2 is the most efficient dissociation pathway for this complex indicates that the structure for this molecule is ZrO^+ ligated by CO_2 rather than a different isomer of $ZrCO_3^+$, e.g. $O_2Zr^+(CO)$. The threshold measured for reaction (15) (Table 4) is assigned to $D_0(OZr^+\text{-}CO_2) = 0.74 \pm 0.06$ eV.

3.7. $O_2Zr^+(CO)$ + Xe

Collision-induced dissociation of the $O_2Zr^+(CO)$ complex yields one product from reaction (16), as shown in Fig. 8.

$$O_2Zr^+(CO) + Xe \rightarrow ZrO_2^+ + CO + Xe \qquad (16)$$

This cross section rises rapidly from an apparent threshold near 0.5 eV. The observation that this product is the only observed decomposition pathway verifies the assignment of the structure of this molecule, ZrO_2^+ ligated by CO. Further, if ZrO_2^+ had a structure of molecular oxygen bound to Zr^+, i.e. $Zr^+(O_2)$, then we would anticipate seeing competitive loss of O_2. Failure to observe this process points to a zirconium dioxide cation. Analysis of the cross section obtained from this reaction (Table 4) gives $D_0(O_2Zr^+\text{-}CO) = 1.01 \pm 0.08$ eV.

3.8. ZrO_2^+ + Xe

Collision-induced dissociation of ZrO_2^+ with Xe gives only one product from reaction (17), as shown in Fig. 9.

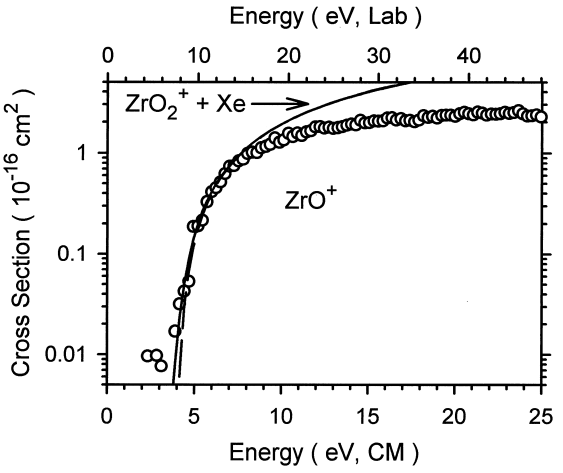

Figure 9. Product cross sections for ZrO_2^+ + Xe as a function of collision energy in the center-of-mass frame (lower *x* axis) and laboratory frame (upper *x* axis). The dashed line is the model of Eq. (1) with the optimized parameters listed in Table 4 for the CID process. The solid line shows this model convoluted over the experimental energy distributions.

$$ZrO_2^+ + Xe \rightarrow ZrO^+ + O + Xe \quad (17)$$

The ZrO^+ cross section rapidly rises from an apparent threshold near 4 eV. Analysis of the energy dependence of this cross section results in $D_0(OZr^+\text{-}O)$ = 3.97 ± 0.20 eV (Table 4). It is possible that this value is an upper limit because previous work done on the CID of diatomic metal oxide cations with Xe has shown the thresholds measured are generally higher than bond energies measured from results for other reactions (e.g. $M^+ + CO$ or $O_2 \rightarrow MO^+ + C$ or O) [48].

4. Discussion

4.1. ZrO_2^+ thermochemistry

From reactions (4), (8), (10), (13), and (17), we can calculate OZr^+-O bond dissociation energies (BDEs) of 3.88 ± 0.24, 3.31 ± 0.13, 3.86 ± 0.07, <5.45, and 3.97 ± 0.20 eV, respectively. These are all consistent with each other with the exception of the value obtained from reaction (8), which is probably too low because this process competes with the favored reaction (6). Overall, we take the BDE of OZr^+-O to be 3.86 ± 0.07 eV, on the basis of the most precise result obtained from reaction (10). This value compares reasonably well with a literature determination of 3.5 ± 0.4 eV [49], which has a precision that is primarily limited by ionization energy measurements.

We can also compare our thermodynamic information for ZrO_2^+ to the literature by deriving the ionization energy (IE) for ZrO_2. Given $\Delta_f H_0(Zr)$ = 602.1 ± 8.4 kJ/mol and $\Delta_f H_0(O)$ = 246.79 ± 0.10 kJ/mol [50], the atomization energies of Murad and Hildenbrand, $D_0(Zr\text{-}2O)$ = 1386 ± 30 kJ/mol [49] and of Chupka et al., $D_0(Zr\text{-}2O)$ = 1399.1 ± 20 kJ/mol [51], yield $\Delta_f H_0(ZrO_2)$ = −290 ± 31 and −303 ± 22 kJ/mol, respectively. Given IE(Zr) = 6.634 eV [52], our bond energies for ZrO^+ and ZrO_2^+ (Table 2) can be combined to yield $\Delta_f H_0(ZrO_2^+)$ = 615 ± 15 kJ/mol. Combining the heats of formation for ZrO_2 and ZrO_2^+, we derive $IE(ZrO_2)$ = 9.38 ± 0.35 and 9.51 ± 0.28 eV, respectively, where the uncertainties are primarily limited by the heat of formation of neutral ZrO_2. This ionization energy is in good agreement with direct determinations by Murad and Hildenbrand [49], 9.4 ± 0.2 eV, and Rauh and Ackermann [53], 9.55 ± 0.1 eV. Indeed, if we combine the latter IE with our value for $\Delta_f H_0(ZrO_2^+)$, we obtain $\Delta_f H_0(ZrO_2)$ = −306 ± 18 kJ/mol, in good agreement with both literature values.

The large decrease in bond energy from the first to the second oxide ligand of ZrO_2^+ parallels results for the isovalent neutrals, YO and YO_2, where $D_0(OY\text{-}O)$ = 4.14 ± 0.22 eV [54] and $D_0(Y\text{-}O)$ = 7.41 ± 0.12 eV [55]. In both the Y and Zr^+ cases, the second metal-oxide bond energy is about half the first. These results are in contrast with the BDEs of the metal oxides and dioxides of Nb^+ and Zr. In previous work, we determined $D_0(Nb^+\text{-}O)$ = 7.13 ± 0.11 eV [48] and $D_0(ONb^+\text{-}O)$ = 5.71 ± 0.17 eV [25], such that the second metal-oxide bond is only 80% of the first. Likewise, $D_0(OZr\text{-}O)$ is 6.3 ± 0.5 eV and $D_0(Zr\text{-}O)$ is 8.00 ± 0.13 eV [55], which again gives an 80% ratio. The difference between the Nb^+ (Zr) and Zr^+ (Y) systems can be understood by looking at the electronic configurations of the metal oxide and dioxides. All four metal monoxides form very strong bonds,

consistent with triple bond formation in which the oxygen donates four electrons, similar to the binding in CO. Both ZrO and NbO^+ have two unpaired electrons such that they can form another strong bond with O in a similar fashion. YO and ZrO^+ have only one unpaired electron, however, such that a second O atom can form at best a double bond, consistent with the much weaker BDEs determined.

4.2. ZrO^+ excitation energies

As noted above, secondary features in the cross sections for reactions (2) and (13) are plausibly assigned to the formation of excited states of ZrO^+. In previous studies of the reactions of metal and metal-oxide cations with CO_2 and their reverse reactions [24,25], we have found that such features can be attributed to an enhanced reaction efficiency at the threshold for a spin-allowed channel. Reactions observed at lower kinetic energies are thermodynamically more favorable, but can be suppressed if they are spin-forbidden. This scenario also seems appropriate for the present cases. For reaction (2), the formation of ground state $ZrO^+(^2\Sigma^+)$ from Zr^+ (a^4F) + $CO_2(^1\Sigma_g{}^+)$ reactants is spin-forbidden, such that production of ZrO^+ might be enhanced if formed in a quartet spin state. ZrO^+ has a $^2\Sigma^+(1\sigma^2 1\pi^4 2\sigma^1)$ ground state configuration, such that the lowest energy quartet state is formed by promoting a bonding π electron into a nonbonding δ orbital, the next highest molecular orbital according to theoretical studies of ZrO [56]. Such a promotion results in $^4\Phi$ and $^4\Pi$ $(1\sigma^2 1\pi^3 2\sigma^1 1\delta^1)$ excited states. For reaction (13), the ground state $ZrO_2{}^+(^2\Sigma^+)$ + $CO(^1\Sigma^+)$ reactants can form the ground state products, $ZrO^+(^2\Sigma^+)$ + $CO_2(^1\Sigma_g{}^+)$, accounting for the exothermic reactivity observed in Fig. 6. The secondary endothermic feature is also assigned to a spin-allowed process to form an excited doublet state of ZrO^+. Excited doublet states can be obtained by simple promotion of the 2σ to the nonbonding 1δ or antibonding 2π orbitals. These excitations would produce $^2\Delta(1\sigma^2 1\pi^4 1\delta^1)$ and $^2\Pi(1\sigma^2 1\pi^4 2\pi^1)$ excited states for ZrO^+.

Although these assignments are not definitive, the thresholds obtained for the endothermic secondary features of reactions (2) and (13) lead to energies 2.93 ± 0.14 and 1.99 ± 0.08 eV higher than the ground states, respectively (Tables 3 and 4). Assuming that there are no barriers in excess of the endothermicity of these reactions, these energies can be assigned as excitation energies for ZrO^+. On the basis of the arguments above, we speculatively assign these energies to the $^4\Phi$ and $^2\Delta/^2\Pi$ states. Some verification of these assignments can be achieved by comparing these excitation energies to those of the isoelectronic neutral YO molecule. Here, excitation to the $^4\Phi$ state has been calculated to be 3.34 eV [56], which is somewhat higher than the 2.93 ± 0.14 eV value measured here. However, this difference may be a result of stabilization of the 1δ (4d-like) orbital upon ionization. Excitations to the $^2\Delta$ and $^2\Pi$ excited states of YO have been calculated to be 1.90 and 1.95 eV, respectively [56], and measured as 1.83 and 2.06 eV, respectively [57]. These are comparable to the 1.99 ± 0.08 eV excitation energy measured here.

4.3. $Zr^+(CO_2)$ potential energy surface

To understand these experiments in more detail, we take the point of view that the experiments performed in this study (Zr^+ + CO_2, ZrO^+ + CO, and OZr^+-CO CID) probe three separate places on the same set of potential energy surfaces for the $Zr^+(CO_2)$ system. The electronic states for the Zr^+ + CO_2 reactants, described in the introduction, are shown in Fig. 10. The measurement of $D_0(OZr^+\text{-}CO)$ determines the well depth of this intermediate for ground state species. The well depth for $Zr^+\text{-}CO_2$ could not be measured in this study, therefore, we estimate the well depth as being slightly less than that of $V^+\text{-}CO_2$, 0.75 ± 0.04 eV [24]. We anticipate the bonding of Zr^+ with CO_2 and ZrO^+ with CO is dominated by donation of ligand electrons into an empty 5s orbital on the metal and backdonation of electron density from metal $4d\pi$ orbitals into empty π-symmetry orbitals of the ligand. Bonding is enhanced when the 5s orbital is empty and the $4d\pi$ orbitals are occupied. Using this argument, we anticipate that Zr^+ states where the 5s orbital is occupied (the a^4F, a^2D, a^2P, a^2F, and a^4P) and ZrO^+ states

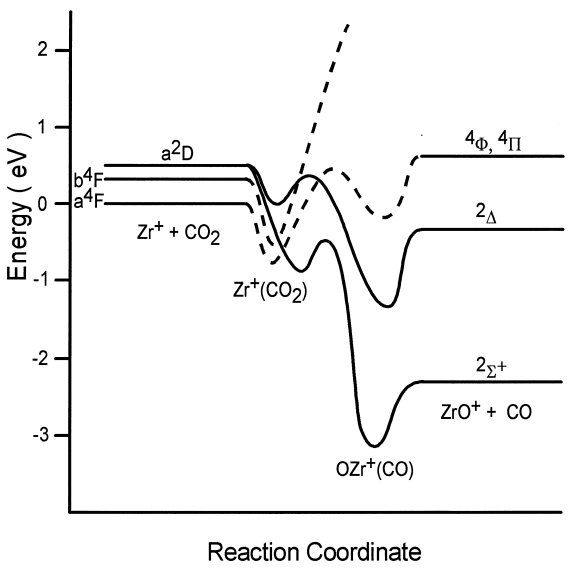

Figure 10. Potential energy surfaces for the interaction of Zr^+ with CO_2 deduced in the present study. Solid lines show doublet surfaces while dashed lines indicate quartet surfaces. Energies of the reactants and ground state product asymptotes and the $OZr^+(CO)$ ground state are shown quantitatively. All other features are estimated. See text.

where the 2σ orbital, which has a great deal of 5s character, is occupied (the $^2\Sigma^+$, $^4\Phi$, and $^4\Pi$) will have smaller bond energies than $Zr^+(b^4F,\ a^2G)$ and $ZrO^+(^2\Delta,\ ^2\Pi)$ states. The strongest bonding between Zr^+ and CO_2 should occur between CO_2 and $Zr^+(a^2G,\ 4d^3)$ because the 5s orbital is empty and 2 electrons can occupy the π backbonding orbital. However, surfaces evolving from this asymptote will have avoided crossings with those evolving from $Zr^+(a^2D) + CO_2$. For simplicity, we show in Fig. 10 only the states of Zr^+ that we believe will be major contributors to the interaction of Zr^+ with CO_2.

The asymptotes of $Zr^+ + CO_2$ and $ZrO^+ + CO$ must now be connected. The lowest energy doublet state of $Zr^+(CO_2)$ correlates adiabatically with $Zr^+(a^2D) + CO_2$ reactants. This state then evolves to ground state $OZr^+(CO)$ and on to $ZrO^+(^2\Sigma^+) + CO(^1\Sigma^+)$ ground state products. These reactants should also correlate with the $ZrO^+(^2\Delta,\ ^2\Pi) + CO(^1\Sigma^+)$ excited state product asymptotes, while $Zr^+(a^4F) + CO_2(^1\Sigma_g{}^+)$ reactants evolve to the $ZrO^+(^4\Phi,\ ^4\Pi) + CO(^1\Sigma^+)$ excited state product asymptotes.

With these potential energy surfaces, we can now understand most of our experimental observations. At the lowest energies, $Zr^+(a^4F)$ reacts with CO_2 to form $ZrO^+(^2\Sigma^+) + CO(^1\Sigma^+)$ in an exothermic spin-forbidden reaction. Because we observe no barrier to the reaction, the transition state between $Zr^+(CO_2)$ and $OZr^+(CO)$ and the quartet–doublet surface crossing must have energies below the $Zr^+(a^4F) + CO_2(^1\Sigma^+{}_g)$ asymptote, Fig. 10. As the kinetic energy is increased, $Zr^+(a^4F)$ reacts to form $ZrO^+ + CO$ more efficiently and this can be attributed to the spin-allowed pathway forming $ZrO^+(^4\Phi,\ ^4\Pi)$.

When $ZrO^+(^2\Sigma^+)$ reacts with CO $(^1\Sigma^+)$, the dominant reaction is simple collision-induced dissociation, although inefficient production of $Zr^+ + CO_2$ is observed. This result suggests that the rearrangements necessary to reform CO_2 are inhibited by the large endothermicity and the transition state involved. Because this reverse reaction is likely to have a similar propensity for conserving spin as does the $Zr^+ + CO_2$ reaction, excited doublet states of Zr^+ may be the primary products in this reaction. This may explain why the apparent threshold for formation of $Zr^+ + CO_2$ is slightly higher than the thermodynamic threshold for forming $Zr^+(a^4F)$, 2.31 ± 0.11 eV. When $OZr^+(CO)$ is collisionally activated, simple CID of the CO ligand dominates the product spectra, Fig. 4. This is clearly because ligand loss is much more facile and energetically favorable than the rearrangements necessary to form $Zr^+ + CO_2$.

4.4. $ZrCO_3^+$ system

In the $ZrCO_3^+$ system, the formation of $ZrO^+ + CO_2$ from $ZrO_2^+ + CO$ reactants is exothermic and reasonably efficient, whereas the reverse reaction is endothermic. These observations are the result of the OZr^+-O bond being weaker than the OC-O bond. In addition, both ZrO^+ and ZrO_2^+ have doublet ground states, such that the formation of CO_2 conserves spin. This behavior is in direct contrast with the reactivity of the bare metal ion, where the reaction of $Zr^+ + CO_2 \rightarrow ZrO^+ + CO$ is exothermic and efficient,

while the reverse process is endothermic. In this case, formation of ground state reactants from ground state products is spin-forbidden. Clearly, the strong difference between the first and second zirconium oxide bond energies (Table 2) leads to this disparate behavior.

5. Summary

We used guided ion beam mass spectrometry to study the kinetic energy dependence of the bimolecular reactions of Zr^+ and ZrO^+ with CO_2 and ZrO^+ and ZrO_2^+ with CO and also the collisional activation of $OZr^+(CO)$, $OZr^+(CO_2)$ and $O_2Zr^+(CO)$ by Xe. Bond energies for several of these species are obtained along with speculative assignments for two excitation energies of ZrO^+.

Acknowledgement

This research is supported by the National Science Foundation, grant no. CHE-9530412.

References

[1] Y. Avila, J. Barrault, S. Pronier, C. Kappenstein, Appl. Catal. 132 (1995) 97.
[2] J. Miciukiewicz, T. Mang, Appl. Catal. 122 (1995) 151.
[3] T. Fujita, Y. Nishiyama, Y. Ohtsuka, K. Asami, K.-I. Kusakabe, Appl. Catal. 126 (1995) 245.
[4] T. Weimer, K. Schaber, M. Specht, A. Bandi, Energy Convers. Management 37 (1996) 1351.
[5] Y. Yanagisawa, Energy Convers. Management 36 (1995) 443.
[6] S.-E. Park, S.S. Nam, M.J. Choi, K.W. Lee, Energy Convers. Management 36 (1995) 573.
[7] M. Saito, T. Fujitani, I. Takahara, T. Watanabe, M. Takeuchi, Y. Kanai, K. Moriya, T. Kakumoto, Energy Convers. Management 36 (1995) 577.
[8] M. Hirano, T. Akano, T. Imai, K. Kuroda, Energy Convers. Management 36 (1995) 585.
[9] D.K. Otorbaev, Chem. Phys. 196 (1995) 543.
[10] M. Sahibzada, D. Chadwick, I.S. Metcalfe, Catal. Today 29 (1996) 367.
[11] D. Gasser, A. Baiker, Appl. Catal. 48 (1989) 279.
[12] C. Schild, A. Wokaun, A. Baiker, J. Molec. Catal. 63 (1990) 243.
[13] Y. Amenomiya, Appl. Catal. 30 (1987) 57.
[14] N.B. Jackson, J.G. Ekerdt, J. Catal. 101 (1986) 90.
[15] M.-Y. He, J.G. Ekerdt, J. Catal. 90 (1984) 17.
[16] M.M. Kappes, R.H. Staley, J. Phys. Chem. 85 (1981) 942.
[17] M.M. Kappes, R.H. Staley, J. Am. Chem. Soc. 103 (1981) 1286.
[18] A.V. Kikthenko, V.B. Goncharov, K.I. Zamaraev, Catal. Lett. 21 (1993) 353.
[19] E.F. Fialko, A.V. Kikthenko, V.B. Goncharov, K.I. Zamaraev, Catal. Lett. 41 (1996) 7.
[20] T.P.J. Izod, G.B. Kistiakowsky, S. Matsuda, J. Chem. Phys. 76 (1972) 2833.
[21] S. Matsuda, J. Chem. Phys. 57 (1972) 807.
[22] S. Matsuda, J. Phys. Chem. 76 (1972) 2833.
[23] R. Wesendrup, H. Schwarz, Angew. Chem. Int. Ed. Engl. 34 (1995) 2033.
[24] M.R. Sievers, P.B. Armentrout, J. Chem. Phys. 102 (1995) 754.
[25] M.R. Sievers, P.B. Armentrout, Int. J. Mass Spectrom., in press.
[26] C.E. Moore, Atomic Energy Levels US GPO Circular No. 467, Washington, DC, 1952.
[27] R.J. Van Zee, S. Li, W. Weltner Jr., Chem. Phys. Lett. 217 (1994) 381.
[28] W.J. Balfour, B. Lindgren, Phys. Scr. 22 (1980) 36.
[29] P.E.M. Siegbahn, J. Phys. Chem. 97 (1993) 9096.
[30] K.M. Ervin, P.B. Armentrout, J. Chem. Phys. 83 (1985) 166.
[31] R.H. Schultz, P.B. Armentrout, Int. J. Mass Spectrom. Ion. Processes 107 (1991) 29.
[32] M.R. Sievers, Y.-M. Chen, J.L. Elkind, P.B. Armentrout, J. Phys. Chem. 100 (1996) 54.
[33] R.H. Schultz, P.B. Armentrout, J. Chem. Phys. 96 (1992) 1046.
[34] R.H. Schultz, K.C. Crellin, P.B. Armentrout, J. Am. Chem. Soc. 113 (1992) 8590.
[35] F.A. Khan, D.E. Clemmer, R.H. Schultz, P.B. Armentrout, J. Phys. Chem. 97 (1993) 7978.
[36] E.R. Fisher, B.L. Kickel, P.B. Armentrout, J. Phys. Chem. 97 (1993) 10204.
[37] N.F. Dalleska, K. Honma, P.B. Armentrout, J. Am. Chem. Soc. 115 (1993) 12125.
[38] N. Aristov, P.B. Armentrout, J. Am. Chem. Soc. 108 (1986) 1806 and references therein.
[39] W.J. Chesnavich, M.T. Bowers, J. Phys. Chem. 83 (1979) 900.
[40] P.B. Armentrout, in Advances in Gas Phase Ion Chemistry, Vol. 1, N.G. Adams, L.M. Babcock (Eds.), JAI: Greenwich, 1992, pp. 83–119.
[41] D_{ex}, ω_x, and μ_x are the dissociation energy, frequencies, and reduced mass for species x.
[42] J.M. Dyke, A.M. Ellis, M. Fehér, A. Morris, A.J. Paul, J.C.H. Stevens, J. Chem. Soc. Faraday. Trans. 2, 83 (1987) 1555.
[43] A.G. Gershikov, V.P. Spiridinov, A. Ya. Prikhod'ko, E.V. Erokhin, High Temp. Sci. 14 (1981) 17.
[44] T. Shimanouchi, Table of Molecular Vibrational Frequencies, Consolidated, Vol. I, National Bureau of Standards, Washington, DC, 1972.
[45] K.P. Huber, G. Herzberg, Molecular Spectra and Molecular

Structure IV. Constants of Diatomic Molecules, Vol. IV, Van Nostrand Reinhold, New York, NY, 1979.
[46] J.M. Dyke, W.J. Gravenor, M.P. Hastings, A. Morris, J. Phys. Chem. 89 (1985) 4613.
[47] L.A. Barnes, M. Rosi, C.W. Bauschlicher Jr., J. Chem. Phys. 93 (1990) 609.
[48] M.R. Sievers, Y.-M. Chen, P.B. Armentrout, J. Chem. Phys. 105 (1996) 6322.
[49] E. Murad, D.L. Hildenbrand, J. Chem. Phys. 63 (1975) 1133.
[50] M.W. Chase, C.A. Davies, J.R. Downey, D.J. Frurip, R.A. McDonald, A.N. Syverud, J. Phys. Chem. Ref. Data 14 (1985) Suppl. No. 1 (JANAF Tables).
[51] W.A. Chupka, J. Berkowitz, M.G. Inghram, J. Chem. Phys. 26 (1957) 1207.
[52] P.A. Hackett, M.R. Humphries, S.A. Mitchell, D.M. Rayner, J. Chem. Phys. 85 (1986) 3194.
[53] E.G. Rauh, R.J. Ackermann, J. Chem. Phys. 60 (1974) 1396.
[54] D.E. Clemmer, N.F. Dalleska, P.B. Armentrout, Chem. Phys. Lett. 190 (1992) 259.
[55] J.B. Pedley, E.M. Marshall, J. Phys. Chem. Ref. Data 12 (1983) 967.
[56] S.R. Langhoff, C.W. Bauschlicher Jr., J. Chem. Phys. 89 (1988) 2160.
[57] C.L. Chalek, J.L. Gole, J. Chem. Phys. 65 (1976) 2845.